The airborne inertially stabilized platform suspend by an axial-radial integrated active magnetic actuator system

Tong Wen [a,d], Biao Xiang [b,c,*]

[a] School of Instrument Science and Optoelectronics Engineering, Beihang University, Beijing 100191, China
[b] School of Mechano-Electronic Engineering, Xidian University, Hi-Tech Development Zone, Xi'an City, Shaanxi Province 710126, China
[c] Department of Mechanical Engineering, The Hong Kong Polytechnic University, Kowloon, Hong Kong, China
[d] Ningbo Institute of Technology, Beihang University, Ningbo, Zhejiang Province 31500, China

HIGHLIGHTS

- A novel structure of AMA system is designed and constructed, and the axial control and radial control are integrated in the AMA system.
- The magnetic forces and the gimbal torques of the axial-radial integrated AMA system have good actively controllability and linearity.
- The good tracking performance of the AMA system is experimentally verified, and mid-frequency disturbance is effectively suppressed.

GRAPHICAL ABSTRACT

The experimental results show that the better attitude stabilization precision and the fast response speed benefit from the contactless suspension and active controllability of the axial-radial integrated AMA system, and it is potential to be applied in the airborne remote sensing system to improve the measurement accuracy.
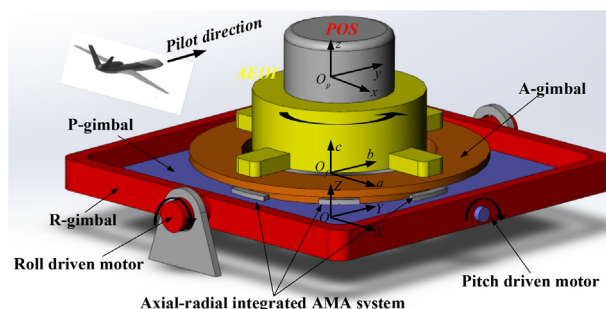
ARTICLE INFO

ABSTRACT

Introduction: The inertial stabilization platform (ISP) is widely used in the earth observation system to stably track the line of sight of the payload because it could isolate vibrations and angular motions of the aviation platform.
Objectives: an active magnetic actuator (AMA) system integrating the axial and the radial control is used to levitate the azimuth gimbal to improve attitude stabilization precision and dynamic performance of the ISP, and then the dynamic model of azimuth gimbal is developed.
Methods: The magnetic force and the gimbal torque of the axial-radial integrated AMA system are investigated, and the attitude information of the suspended azimuth gimbal is measured.
Results: The attitude stabilization precision of azimuth gimbal is confined at 0.02°, and the control bandwidth of the axial-radial integrated AMA system could exceed 100 Hz.
Conclusion: the ISP with an axial-radial integrated AMA system has better attitude stabilization precision and wider control frequency than the pure mechanical ISP, so it is potential to be applied in the airborne remote sensing system to improve the measurement precision.
© 2021 The Authors. Published by Elsevier B.V. on behalf of Cairo University. This is an open access article under the CC BY-NC-ND license (http://creativecommons.org/licenses/by-nc-nd/4.0/).

Introduction

The aviation earth observation instruments (AEOI) such as the large format CCD (charge coupled device) aerial camera and the hyperspectral image radiometer are installed on the inertial stabilization platform (ISP) to isolate the vibrations and angular motions of the aviation platform. For the normal ISP with mechanical bearings and gears, the disturbance isolation ability is determined by the control performance of the servo-drive system and the mechanical vibration isolation system [1–3]. In general, the triple-gimbal configuration including an azimuth gimbal (A-gimbal), a roll gimbal (R-gimbal) and a pitch gimbal (P-gimbal) is widely adopted in the pure mechanical ISP whose gimbals are supported by the rolling bearings [4–7], and the rotations of three gimbals due to the aviation platform are isolated from the inside to outside by the mechanical vibration isolation system. Nevertheless, the friction of ball bearings and the gear transmission error of servo-drive system would weaken the vibration isolation performance, and then control precisions and dynamic characteristics of the traditional ISP with the mechanical vibration isolator are affected [8–10].

The major research on the pure mechanical ISP are focused on improving the control precision and the dynamic response of the servo-drive system. Numerous methods have been successfully applied into the control engineering of the pure mechanical ISP. In general, the decoupling control [11,12] was the common method to suppress the coupling effect among different gimbals in the pure mechanical ISP [13], and then the attitude stabilization precision of each gimbal could be improved. For example, a decoupling model based on an inverse system was used to transfer the nonlinear system of a two-axis ISP into a pseudo-linear system [11], and the coupling multi-input multi-output system was transferred into two decoupling single-input single-output systems. The experimental results showed that the attitude stabilization precision of two-axis ISP was improved from 0.03° with PID control to 0.015°. Moreover, the robust control method was also tried to be applied in the control engineering of the pure mechanical ISP system [14–20], and the major function of the robust control scheme was to attenuate the parameter uncertainties such as the frictions of rolling bearings, the transmission errors and mismatches of gear pairs. In reference [18,21], a robust feedback tracking model incorporated with a modified extended state observer (ESO) was applied to improve the tracking performance of the ISP system in the presence of mass imbalance, kinematic coupling, carrier vibrations and external disturbances. The simulation results presented that the maximum absolute value of speed tracking error was reduced from 1.261°/s to 0.974°/s. A nonlinear second-order ESO [22] was designed to compensate the composite disturbances, and the maximum deflection of azimuth gimbal was reduced to 0.06°. In addition, the disturbance observer was also designed to the control engineering of pure mechanical ISP system [23–25], and the attitude stabilization precisions of controlled gimbals were obviously enhanced.

For pure mechanical ISP systems in those above-mentioned publications, the vibration phenomenon and the control error were primarily caused by the frictions of rolling bearings, the mismatches of gear pairs and the external disturbances. Although those above-mentioned control models used in the pure mechanical ISP system could improve the attitude stabilization precisions of controlled gimbals, the disturbance sources could not be eliminated. Therefore, the disturbance sources would lead to other kinds of influences on gimbals when the operational status of pure mechanical ISP changes.

Moreover, for the pure mechanical ISP system, the disturbances with a high frequency (greater than 10 Hz) could be suppressed by the mechanical vibration isolator, and the disturbances with a low-frequency (below 2 Hz) could be compensated by the rotational torques of gimbals driven by the servo-drive system. However, the residual disturbances with a mid-frequency (from 2 Hz to 10 Hz) could not effectively suppressed by the mechanical vibration isolator and the servo-drive system. So, a new structure is necessary to be designed in the ISP system to mitigate the mid-frequency disturbances.

The magnetic suspension technology had been successfully used to suspend the rapidly spinning rotors such as flywheel [26–28], turbine machine vacuum pump [29–31] and so on. The benefits such as micro vibration and tinny friction are brought out by the advantage of contactless suspension. The other advantages are the fast response and the attitude adjusting ability of the suspended object within the tiny airgap. Obviously, it is potential to be integrated in the ISP system to improve the attitude stabilization precision of the observation instruments mounted on the ISP. As a practical application of the magnetic suspension technology, the active magnetic actuator (AMA) has advantages on the fast response and active controllability [32], and the mid-frequency disturbances could be depressed by the AMA too. Moreover, the attitude precision of AEOI could be regulated to reach better stabilization precision because of the tunable airgap between the AMA and the suspended object.

In this article, a prototype of magnetically suspended ISP (MS-ISP) with an axial-radial integrated AMA system is designed to improve the attitude stabilization precision. The inner A-gimbal is suspended by an axial-radial integrated AMA system on five degrees of freedom (DOFs). The residual mid-frequency disturbances could be depressed by the magnetic forces and the gimbal torques of the axial-radial integrated AMA system, and the attitude stabilization precisions of the observation instruments mounted on the A-gimbal could be improved furthermore. The main features of designed MS-ISP are listed as following

1. A novel structure of AMA system is designed and constructed, and the axial control and radial control are integrated in the AMA system, so the volume of AMA system is greatly minimized.
2. The good tracking performance of the AMA system is experimentally verified, and mid-frequency disturbance (2 Hz-10 Hz) is effectively suppressed by the force of AMA system.
3. This article is organized as follows. Firstly, the configuration of MS-ISP is described in section 2. The dynamics of A-gimbal is developed in section 3. The control strategy and the control system are represented in section 4. Finally, the simulation and experimental results of the designed MS-ISP are analyzed in section 5. The experimental results show that the better attitude stabilization precision and the fast response speed benefit from the contactless suspension and active controllability of axial-radial integrated AMA system.

Structure of MS-ISP

As shown in Fig. 1, the MS-ISP consists of three rotational gimbals, an axial-radial integrated AMA system, three pairs of eddy current gap sensors (ECGS), a position and orientation system (POS), a main control unit (MCU). The AEOI is fixed on the A-gimbal of MS-ISP, and the POS is mounted on the AEOI to measure the attitude information of A-gimbal in the geographic coordinate frame. The motions caused by the aviation platform would be easily transferred to the AEOI, and further distort the line of sight (LOS) of AEOI. Therefore, through the servo-drive control of three gimbals and the active suspension control of axial-radial integrated AMA system, the MS-ISP is used to stably track the LOS of AEOI vertically pointing to the earth's surface.
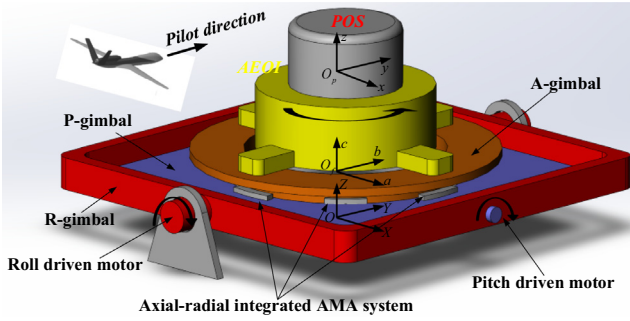
Fig. 1. The sketch of MS-ISP with an axial-radial integrated AMA system.

The gimbal system of MS-ISP

For three gimbals of the MS-ISP as shown in Fig. 1, the outer one is R-gimbal, and it depresses the roll motion of MS-ISP. The middle one is P-gimbal which could isolate the pitch motion of MS-ISP. Finally, the inner one is the A-gimbal, which could attenuate the yaw motion of MS-ISP. The major difference between the MS-ISP and the pure mechanical ISP is that the inner A-gimbal is levitated by an axial-radial integrated AMA system. Expect the yaw motion of A-gimbal controlled by the servo-drive motor, the contactless suspension of A-gimbal on other five DOFs are realized by magnetic forces and gimbal torques of axial-radial integrated AMA sys-

tem. Therefore, the A-gimbal with an axial-radial integrated AMA system has more five controllable DOFs than the mechanical gimbal with rolling bearings, and the disturbances acting on the five controllable DOFs could be suppressed by magnetic forces and gimbal torques of the axial-radial integrated AMA system.

The structure of A-gimbal with an axial-radial integrated AMA system is shown in Fig. 2. The stator part of axial-radial integrated AMA system is mounted on the P-gimbal with reasonable airgaps in axial and radial directions. Then, the attitudes and positions of A-gimbal relative to P-gimbal could be regulated within the reasonable airgaps in axial and radial directions, and the LOS of AEOI could be tunable further by using the adjustable attitude information of A-gimbal about rotations around R-gimbal and P-gimbal.

In the meanwhile, according to the motion status of A-gimbal with an axial-radial integrated AMA system as shown in Fig. 3, the translational displacements $[d_{xe}\ d_{ye}\ d_{ze}]$ represent the translational positions of A-gimbal relative to P-gimbal along three axes, and the rotational angles $[\alpha_e\ \beta_e]$ represent the attitude angles of A-gimbal around R-gimbal and P-gimbal, respectively. The displacement terms $[d_{xe}\ d_{ye}\ d_{ze}\ \alpha_e\ \beta_e]$ of A-gimbal are measured by the ECGSs fixed on the P-gimbal. In the control engineering of A-gimbal with an axial-radial integrated AMA system, the displacement terms $[d_{xe}\ d_{ye}\ d_{ze}]$ are hold at the equilibrium statuses by the magnetic forces $[f_x\ f_y\ f_z]$ of axial-radial integrated AMA system. With the function of gimbal torques $[p_x\ p_y]$ of axial-radial integrated AMA system, the attitude angles $[\alpha_e\ \beta_e]$ are forced to track the reference attitudes to isolate the vibrations transferred from the rotations around R-gimbal and P-gimbal.

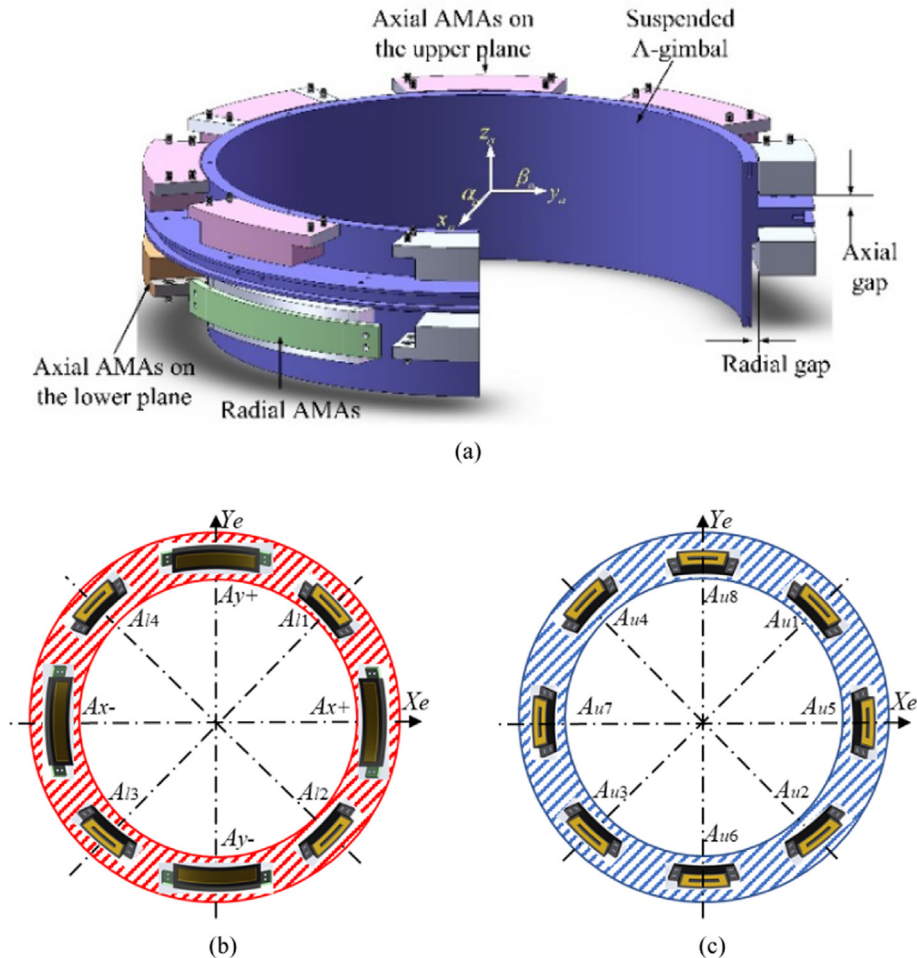

(a)

(b)

(c)

Fig. 2. (a) The prototype of axial-radial integrated AMA system, (b) the lower end-face of P-gimbal with four axial AMAs and four radial AMAs, (c) the upper end-face of P-gimbal with eight axial AMAs.
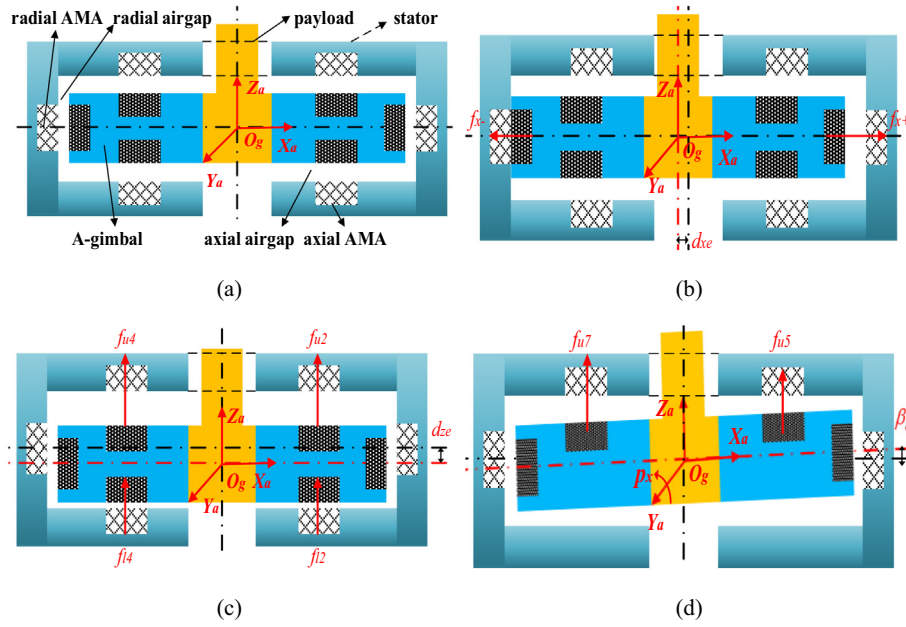
Fig. 3. The motion status of A-gimbal suspended by an axial-radial integrated AMA system, (a) the balanced status of A-gimbal, (b) the translational motion of A-gimbal in radial direction, (c) the translational motion of A-gimbal in axial direction, (d) the rotational motion of A-gimbal around radial axis.

The axial-radial integrated AMA system

An axial-radial integrated AMA system with twelve AMAs in axial direction and four AMAs in radial direction are designed to levitate the massive payloads including the A-gimbal, the AEOI and the POS. In detail, the twelve AMAs in axial direction are distributed as the form of four AMAs ($A_{l1} \sim A_{l4}$) at lower end-face as shown in Fig. 2(b) and eight AMAs ($A_{u1} \sim A_{u8}$) at upper end-face in Fig. 2(c). The positions of four AMAs (A_{x+}, A_{x-}, A_{y+} and A_{y-}) in radial direction are on lower end-face of P-gimbal as illustrated in Fig. 2(b).

As shown in Fig. 3(a), for the motion control of A-gimbal in radial direction, the AMAs A_{x+} and A_{x-} generate magnetic force f_x to suspend A-gimbal at the equilibrium position along X_e axis, and the AMAs A_{y+} and A_{y-} generate magnetic force f_y to suspend A-gimbal at the equilibrium position along Y_e axis. As illustrated in Fig. 3(c) and (d), the twelve AMAs in axial direction are separated into two groups to generate the magnetic force f_z in axial direction and the gimbal torques $[p_x \ p_y]$ around Y_e axis and X_e axis. In detail, the four pairs of axial AMAs (A_{l1}-A_{u1}, A_{l2}-A_{u2}, A_{l3}-A_{u3} and A_{l4}-A_{u4}) at lower and upper end-faces provide magnetic forces to stably suspend the A-gimbal at the axial equilibrium position, and other four axial AMAs generate gimbal torques to isolate the rotations of A-gimbal around Y_e axis and X_e axis. The relation between the generalized magnetic forces and the gimbal torques $[f_x \ f_y \ f_z \ p_x \ p_y]$ of axial-radial integrated AMA system could be expressed into

$$\begin{cases} f_x = f_{x+} + f_{x-} \\ f_y = f_{y+} + f_{y-} \\ f_z = \sum\limits_{i=1}^{4} f_{ui} + \sum\limits_{i=1}^{4} f_{li} \\ p_x = (f_{u5} + f_{u6}) \cdot l_s \cdot \sin\frac{\pi}{4} - (f_{u7} + f_{u8}) \cdot l_s \cdot \sin\frac{\pi}{4} \\ p_y = (f_{u5} + f_{u8}) \cdot l_s \cdot \cos\frac{\pi}{4} - (f_{u6} + f_{u7}) \cdot l_s \cdot \cos\frac{\pi}{4} \end{cases} \tag{1}$$

where, f_{x+}, f_{x-}, f_{y+} and f_{y-} are the radial magnetic forces provided by four radial AMAs. The $f_{u1} \sim f_{u8}$ are the axial magnetic forces provided by the AMAs $A_{u1} \sim A_{u8}$ at upper end-face, and the $f_{l1} \sim f_{l4}$ are the

magnetic forces provided by the four axial AMAs $A_{l1} \sim A_{l4}$ at lower end-face.

Therefore, the displacement terms $[d_{xe} \ d_{ye}]$ are dominated by the four AMAs (A_{x+}, A_{x-}, A_{y+} and A_{y-}) in radial direction, and the displacement terms $[\alpha_e \ \beta_e \ d_{ze}]$ are dominated by the twelve AMAs in axial direction. The eight axial AMAs form into four pairs of AMAs to provide magnetic forces in Z_e axis, and other four AMAs generate magnetic forces to adjust gimbal torques about $[\alpha_e \ \beta_e]$.

The sensors and coordinate frames of MS-ISP

Since the axial-radial integrated AMA system is unstable naturally, the closed-loop control with displacement feedback is needed to realize the stable suspension of A-gimbal in axial and radial directions. So, attitude angles and dynamic positions of A-gimbal should be measured timely and fed back to the closed-loop control system of axial-radial integrated AMA system. Moreover, to adjust the direction of the LOS of AEOI by tracking the reference attitude angles, the attitude angles of A-gimbal relative to the geographic coordinate frame should be also measured timely. Once the attitude angles of A-gimbal are adjusted to tack the reference attitudes in the geographic coordinate frame, the posture of P-gimbal would be achieved through the coordinate transformation.

There are three major sensor systems equipped in the MS-ISP to measure attitude information and dynamic positions of A-gimbal in different coordinate frames. The attitude information and the dynamic positions of the AEOI in the geographic coordinate frame are measured by the POS, and the attitude information of A-gimbal relative to P-gimbal is measured by the ECGS. The attitude information of P-gimbal is measured by the sensors such as gyros, accelerometers located on R-gimbal and P-gimbal. In the meanwhile, three rotation transformation matrices are used to calculate the posture information of airplane based on the posture of inner A-gimbal measured by the POS.

The major coordinate frames of MS-ISP are shown in Fig. 4(b). $OX_bY_bZ_b$ is the coordinate frame fixed on the airplane, $OX_rY_rZ_r$ is the coordinate frame located at the R-gimbal, $OX_pY_pZ_p$ is the coordinate system located at the P-gimbal, $O_gX_eY_eZ_e$ is the coordinate frame fixed on the A-gimbal and $O_gX_gY_gZ_g$ is the geographic coordi-
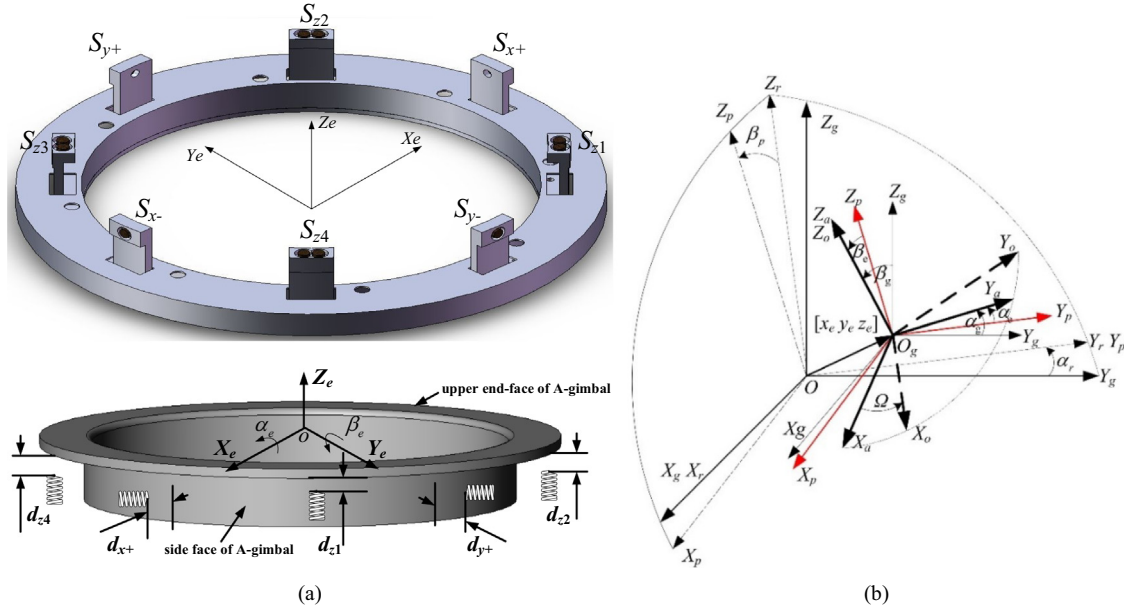
Fig. 4. (a) The axial and radial ECGSs, (b) the coordinate frames of MS-ISP.

nate frame. The translational displacements $[d_{xe}\ d_{ye}\ d_{ze}]$ of A-gimbal are defined by the origin O of P-frame $OX_pY_pZ_p$. The attitude angles $[\alpha_e\ \beta_e]$ of A-gimbal relative to P-frame are defined by the Euler-angle between the frame $O_gX_aY_aZ_a$ and the frame $OX_pY_pZ_p$. The yaw angle of A-gimbal is defined by the Euler-angle between the frame $O_gX_oY_oZ_o$ and the frame $O_gX_aY_aZ_a$ and controlled by the servo-drive motor, which is independent from the axial-radial integrated AMA system. $[\alpha_g\ \beta_g]$ are the posture angles of A-gimbal relative to the geographic coordinate frame. $[\alpha_r\ \beta_p]$ represent the postures of P-gimbal in the geographic coordinate frame, and they could be regarded as the tracking residual to be suppressed in the rotational control of A-gimbal.

A multi-channel ECGS system in Fig. 4(a) is equipped in the MS-ISP to measure the dynamic displacements of suspended A-gimbal. The four axial ECGSs S_{x+}, S_{x-}, S_{y+} and S_{y-} measure the radial displacements of A-gimbal, and four radial ECGSs S_{z1}, S_{z2}, S_{z3} and S_{z4} measure the axial displacements of A-gimbal by detecting upper end-face of A-gimbal. The dynamic displacements $[d_{xe}\ d_{ye}\ d_{ze}\ \alpha_e\ \beta_e]$ measured by the ECGSs are expressed as

$$\begin{cases} d_{xe} = d_{x+} - d_{x-} \\ d_{ye} = d_{y+} - d_{y-} \\ d_{ze} = d_{z1} + d_{z2} + d_{z3} + d_{z4} \\ \alpha_e = \frac{(d_{z1} - d_{z3})}{l_s} \\ \beta_e = \frac{(d_{z2} - d_{z4})}{l_s} \end{cases} \tag{2}$$

The linearity of designed ECGS is 1 mm and the sensitivity is better than 1 μm, and then the sensitivity of ECGS is 3 V/mm. The span l_s of axial ECGSs is 450 mm. Therefore, the angular sensitivity of A-gimbal measured by the EGCS is better than $2.5° \times 10^{-4}$. The bandwidth of ECGS is above 1000 Hz, and much wider than the bandwidth (about 100 Hz) of closed-loop control system.

Dynamic model of the suspended A-gimbal

The magnetic force of axial-radial integrated AMA

Since the AEOI and the POS suspended by the axial-radial integrated AMA system are massive, the power consumption would be great if the magnetic forces are entirely generated by the control current of AMA system. To reduce the power consumption, the permanent magnet (PM) is used in the axial-radial integrated AMA system to provide the bias magnet fluxes, and this kind of AMA structure is defined as PM biased AMA. The bias magnet fluxes without needing power consumption could generate the bias magnetic force for the suspension of A-gimbal and AEOI payloads, so the power consumption is reduced with 90%.

Based on the structure of single AMA as shown in Fig. 5(a), the magnet flux path of axial AMA at upper end-face is plotted in Fig. 5(c). The magnet fluxes of bias PM are marked by yellow solid line, and pass inner and outer ferromagnetic steels on stator, primary airgap between rotor and stator. Moreover, as illustrated as red dash line, the magnet fluxes of control currents pass inner and outer ferromagnetic steels on stator, primary airgap between rotor and stator, the rotor part and the secondary airgap, and this magnet fluxes generated by the control currents are defined as the electromagnetic (EM) magnet fluxes.

Furthermore, the magnetic force could be calculated by using the equivalent magnet circuit as shown in Fig. 6(a) and (b). The equivalent magnet circuit of PM magnet flux is plotted in Fig. 6(a), and the equivalent magnet circuit of EM magnet flux is shown in Fig. 6(b). The magnetic potential of PM flux is

$$F_{pm1} = H_c h_{pm} \tag{3}$$

where H_c is coercive force, and h_{pm} is the length of the bias PM along the magnetization direction.

The magnetic densities of PM magnet circuit in Fig. 6(a) are

$$\begin{cases} \phi_{pm1} = \frac{F_{pm1}}{R_{pmsum1} \cdot \sigma} \\ \phi_{px1} = \frac{\phi_{pm1} \cdot (R_{pmsum1} - R_{pm1})}{R_{11}} \\ \phi_{pwn1} = \frac{\phi_{pm1} \cdot (R_{pmsum1} - R_{pm1})}{R_{w1} + R_{n1}} \end{cases} \tag{4}$$

where R_{pm1} is the magnetic conductance of bias PM, and R_{11} is the magnetic conductance of ferromagnetic steel. R_{w1} and R_{n1} are the magnetic conductance of outer and inner primary airgaps, respectively. R_{pmsum1} is the magnetic conductance of PM magnet circuit. They are expressed as
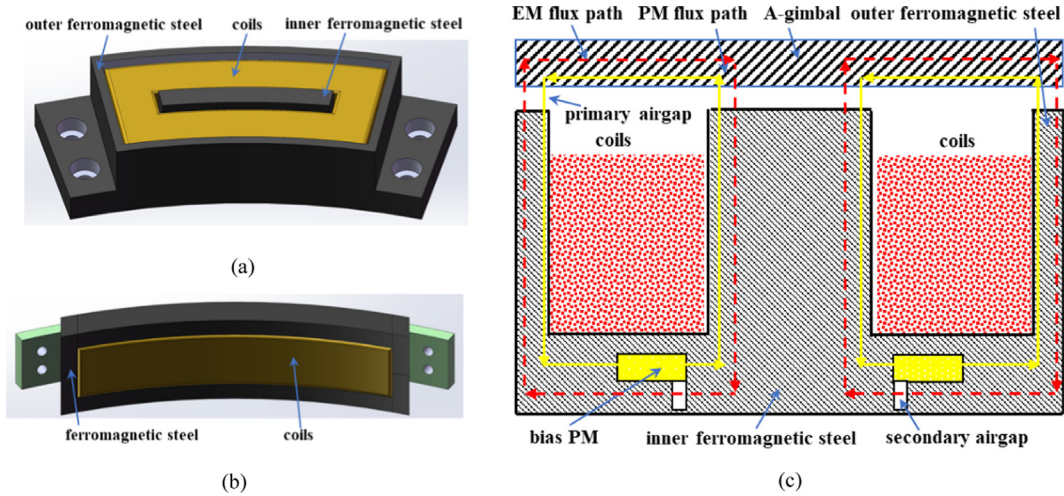
Fig. 5. (a) The stator of axial AMA, (b) the stator of radial AMA, (c) the magnet flux path of axial-radial integrated AMA at upper end-face in axial direction.
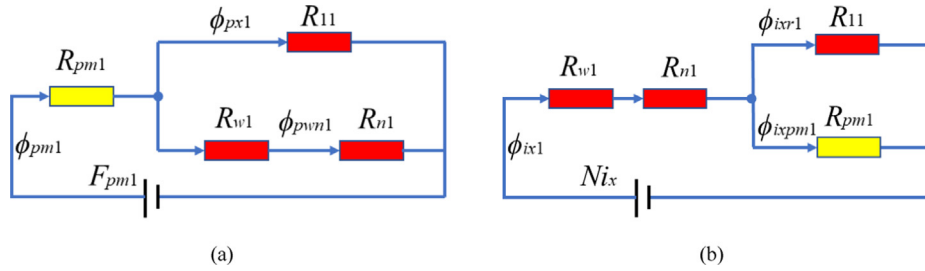

Fig. 6. (a) The equivalent magnet circuit of PM magnet fluxes, (b) the equivalent magnet circuit of EM magnet fluxes.

$$\begin{cases} R_{pmsum1} = R_{pm1} + \frac{1}{\frac{1}{R_{11}} + \frac{1}{R_{w1}+R_{n1}}} \\ R_{pm1} = \frac{h_{pm}}{\mu_0 \mu_r A_{pm}} \\ R_{11} = \frac{\delta_{11}}{\mu_0 A_{11}} \\ R_{w1} = \frac{\delta_{w1}}{\mu_0 A_w} \\ R_{n1} = \frac{\delta_{n1}}{\mu_0 A_n} \end{cases} \tag{5}$$

where A_{pm} is the sectional area of bias PM. μ_r is the relative permeability of bias PM. μ_0 is the vacuum permeability. δ_{11}, δ_{w1} and δ_{n1} are the lengths of corresponding airgaps.

The magnetic densities of EM magnet circuit in Fig. 6(b) are

$$\begin{cases} \phi_{ix1} = \frac{Ni_x}{R_{isumx1}\sigma_e} \\ \phi_{ixr1} = \phi_{ix1} \cdot \frac{R_{isumx1}-R_{w1}-R_{n1}}{R_{11}} \\ \phi_{ixpm1} = \phi_{ix1} \cdot \frac{R_{isumx1}-R_{w1}-R_{n1}}{R_{pm1}} \end{cases} \tag{6}$$

where i_x is the control current of winding, and N is the number of turns of winding. R_{isumx1} is the magnetic conductance of EM magnet circuit in Fig. 5(b), and it could be written into

$$R_{isumx1} = R_{w1} + R_{n1} + \frac{1}{\frac{1}{R_{11}} + \frac{1}{R_{pm1}}} \tag{7}$$

The magnetic density of the axial-radial integrated AMA system in the airgap is the sum of PM magnet flux and EM magnet flux as following

$$\phi_{x1} = \phi_{pwn1} + \phi_{ix1} \tag{8}$$

So, the magnetic force generated by the one pair of axial AMAs at upper end-face is

$$f_{u1} = F_{n1} + F_{w1} = \frac{\phi_{x1}^2}{2\mu_0 A_n} + \frac{\phi_{x1}^2}{2\mu_0 A_w} \tag{9}$$

where A_n and A_w are the sectional areas of inner and outer ferromagnetic steels, respectively.

The magnetic force is nonlinear both with the control displacement and the control current within wide displacement range, but the magnetic force could be linearized within the small vicinity of the equilibrium position. For the convenience of the control engineering of the axial-radial integrated AMA system, the twelve AMAs in axial direction are designed with same current stiffness and displacement stiffness, and the four AMAs in radial direction are designed with the same principle. Furthermore, the magnetic force generated by the one pair of axial AMAs could be expressed as

$$f_z = k_{iz}i_z + k_{dz}d_{ze} \tag{10}$$

The magnetic forces generated by the radial AMAs could be expressed into

$$\begin{cases} f_x = k_{ix}i_x + k_{dx}d_{xe} \\ f_y = k_{iy}i_y + k_{dy}d_{ye} \end{cases} \tag{11}$$

where k_{iz} is the axial current stiffness and k_{dz} is the axial displacement stiffness. $k_{ix} = k_{iy}$ is the radial current stiffness and $k_{dx} = k_{dy}$ is the radial displacement stiffness.

Combing (1), (2) and (10), the gimbal torques $[p_x\ p_y]$ of the axial-radial integrated AMA system could be obtained as following

$$\begin{cases} p_x = (k_{iz}i_{z5} + k_{dz}l\alpha_e + k_{iz}i_{z6} - k_{dz}l\beta_e) \cdot \\ l - (k_{iz}i_{z7} - k_{dz}l\alpha_e + k_{iz}i_{z8} + k_{dz}l\beta_e) \cdot l \\ p_y = (k_{iz}i_{z5} + k_{dz}l\alpha_e + k_{iz}i_{z8} + k_{dz}l\beta_e) \cdot \\ l - (k_{iz}i_{z6} - k_{dz}l\beta_e + k_{iz}i_{z7} - k_{dz}l\alpha_e) \cdot l \end{cases} \quad (12)$$

where $k_{ipx} = k_{ipy}$ is the current stiffness of gimbal torque, $k_{dpx} = k_{dpy}$ is the displacement stiffness of gimbal torque.

The dynamic model of suspended A-gimbal

The dynamics models of A-gimbal are separated into two parts. On the one hand, the translational model in the displacement terms $[d_{xe}\ d_{ye}\ d_{ze}]$ are

$$\begin{cases} m\ddot{d}_{xe} = f_x \\ m\ddot{d}_{ye} = f_y \\ m\ddot{d}_{ze} = f_z \end{cases} \quad (13)$$

On the other hand, the models about two rotational angles $[\alpha_e\ \beta_e]$ and the yaw angle θ_e of A-gimbal are expressed into

$$\begin{bmatrix} \alpha_e \\ \beta_e \\ \theta_e \end{bmatrix} = C_p^a C_r^p C_g^r \begin{bmatrix} \alpha_g \\ \beta_g \\ \theta_g \end{bmatrix} + C_p^a C_r^p \begin{bmatrix} 0 \\ \alpha_r \\ 0 \end{bmatrix} + C_p^a \begin{bmatrix} \beta_p \\ 0 \\ 0 \end{bmatrix} + \begin{bmatrix} 0 \\ 0 \\ \theta_a \end{bmatrix} \quad (14)$$

where θ_a is yaw angle, the coordinate transformation matrices are respectively

$$C_g^r = \begin{bmatrix} \cos\alpha_r & 0 & \sin\alpha_r \\ 0 & 1 & 0 \\ -\sin\alpha_r & 0 & \cos\alpha_r \end{bmatrix}; \quad C_r^p = \begin{bmatrix} 1 & 0 & 0 \\ 0 & \cos\beta_p & -\sin\beta_p \\ 0 & \sin\beta_p & \cos\beta_p \end{bmatrix};$$
$$C_p^a = \begin{bmatrix} \cos\theta_a & \sin\theta_a & 0 \\ -\sin\theta_a & \cos\theta_a & 0 \\ 0 & 0 & 1 \end{bmatrix} \quad (15)$$

Furthermore, the rotational angles $[\alpha_e\ \beta_e]$ could be solved as

$$\begin{bmatrix} \alpha_e \\ \beta_e \end{bmatrix} = \begin{bmatrix} \cos\theta_a\cos\alpha_r + \sin\theta_a\sin\beta_p\sin\alpha_r & \sin\theta_a\cos\beta_p & \cos\theta_a\sin\alpha_r - \sin\theta_a\sin\beta_p\cos\alpha_r \\ -\sin\theta_a\cos\alpha_r + \cos\theta_a\sin\beta_p\sin\alpha_r & \cos\theta_a\cos\beta_p & -\sin\theta_a\sin\alpha_r - \cos\theta_a\sin\beta_p\cos\alpha_r \end{bmatrix}$$
$$\begin{bmatrix} \alpha_g \\ \beta_g \\ \theta_g \end{bmatrix} + \begin{bmatrix} \cos\alpha_r & 0 & \sin\alpha_r \\ \sin\beta_p\sin\alpha_r & \cos\beta_p & -\sin\beta_p\cos\alpha_r \end{bmatrix} \begin{bmatrix} 0 \\ \alpha_r \\ 0 \end{bmatrix} + \begin{bmatrix} \cos\theta_a & \sin\theta_a & 0 \\ -\sin\theta_a & \cos\theta_a & 0 \end{bmatrix} \begin{bmatrix} \beta_p \\ 0 \\ 0 \end{bmatrix} \quad (16)$$

Moreover, the attitude information of MS-ISP on yaw, pitch and roll rotations could be measured by the POS, so the rotational angles $[\alpha_e\ \beta_e]$ could be achieved timely based on the attitude information of other gimbals.

The rotational functions of the axial-radial integrated AMA system around X_e axis and Y_e axis could be written into

$$\begin{cases} J_x\ddot{\alpha}_e + J_z\Omega\dot{\beta}_e = p_x \\ J_y\ddot{\beta}_e - J_z\Omega\dot{\alpha}_e = p_y \end{cases} \quad (17)$$

where Ω is yaw rotational speed of A-gimbal controlled by the servo-drive motor, J_x and J_y are the moment of inertial around X_e and Y_e axis, respectively, and J_z is the moment of inertial around Z_e axis.

Control model of MS-ISP

Control system of MS-ISP

Due to the positive stiffness of magnetic force provided by the axial-radial integrated AMA system, the suspension control of A-gimbal is unstable naturally. It means that a feedback loop is required to realize the stable suspension of A-gimbal. And then, to realize the translational control of A-gimbal, an additional closed-loop tracking system is needed. For the closed-loop control system of A-gimbal's axial and radial translations in Fig. 7(a), the translational displacements $[d_{xe}\ d_{ye}\ d_{ze}]$ of A-gimbal measured by the ECGSs are fed back to the stabilization control loop, and the corresponding control currents $[i_x\ i_y\ i_z]$ are generated to drive the axial-radial integrated AMA system, so the A-gimbal is finally suspended at the center position. For the closed-loop control system of A-gimbal's pitch and roll rotations shown in Fig. 7(b), the MS-ISP should track the reference attitude instructions of pitch and roll rotations to adjust the LOS, so the rotational angles $[\alpha_e\ \beta_e]$ of A-gimbal could deflect from the balanced statues. Therefore, the tracking control loop is added in the posture tracking of A-gimbal. The attitude angles $[\alpha_g\ \beta_g]$ in the geographic coordinate frame is used as the feedback signal in the tracking control loop, and then the gimbal torques $[p_x\ p_y]$ are generated to mitigate the pitch and roll rotations of A-gimbal.

Stability analysis of closed-loop system

For the stability analysis of the axial-radial integrated AMA system, the displacement control d_{xe} in X_e axis is chosen as the analysis example. Based on the negative feedback about the control displacement and the PD control model about the control voltage, the relationship between control current and displacement of axial-radial integrated AMA system could be expressed as

$$i_{xe} = -\left(K_P d_{xe} + K_D \dot{d}_{xe}\right) \cdot k_s k_a \quad (18)$$

where K_P is the proportional coefficient, and K_D is the derivative coefficient. k_s is the sensitivity of ECGS in Fig. 4(a). k_a is the amplification coefficient to drive the windings of axial-radial integrated AMA system.

Combining the force equation in (11), the dynamic equation of AMA system in (13) and the current equation in (18), the equation of axial-radial integrated AMA in X_e axis could be written as

$$m\ddot{d}_{xe} + k_{ix}k_a k_s K_D \dot{d}_{xe} + (k_{ix}k_a k_s K_P - k_{dx})d_{xe} = 0 \quad (19)$$

To guarantee the translational stability of the axial-radial integrated AMA system in X_e axis, the control parameters of PD model should satisfy the following conditions

$$\begin{cases} K_P > \frac{k_{dx}}{k_{ix}k_a k_s} \\ K_D > 0 \end{cases} \quad (20)$$

Therefore, the stability of axial-radial integrated AMA system could be ensured by regulating the parameters of PD model when the system parameters are known.

Stabilization control of closed-loop system

The magnetic force is a function both of the control displacement and the control current, the main task of stabilization control model is to calculate the generalized control signals $U_I = [U_{ix}\ U_{iy}\ U_{iz}\ U_{i\alpha}\ U_{i\beta}]$ according to the feedback displacements $X_e = [d_{xe}\ d_{ye}\ d_{ze}\ \alpha_e\ \beta_e]$ measured by the ECGSs. The U_I are magnified by the power amplification model to generate driving currents I to generate
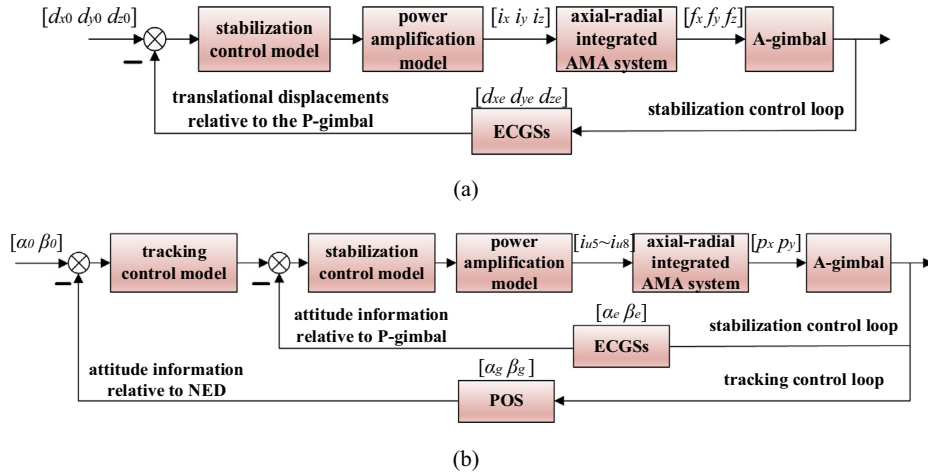
Fig. 7. (a) The closed-loop control system of axial-radial integrated AMA with translations on three DOFs, (b) the closed-loop control system of axial-radial integrated AMA with rotations on two DOFs.

the magnetic forces. The control signals calculated from the PD control model are

$$\boldsymbol{U_I} = k_p \boldsymbol{X}_e + k_d \frac{d}{dt} \boldsymbol{X}_e \tag{22}$$

The control signals should be optimally assigned to the sixteen AMA windings in axial and radial directions as following

$$\begin{cases} U_{ix+} = -U_{ix-} = \frac{U_{ix}}{2} \\ U_{iy+} = -U_{iy-} = \frac{U_{iy}}{2} \\ U_{uj} = \frac{(1-k)\cdot U_{iz}}{2} + \frac{U_{i\alpha}}{2}, & (j = 5,7) \\ U_{uj} = \frac{(1-k)\cdot U_{iz}}{2} + \frac{U_{i\beta}}{2}, & (j = 6,8) \\ U_{uj} = -U_{lj} = \frac{k\cdot U_{iz}}{4}, & (j = 1,2,3,4) \end{cases} \tag{23}$$

where k is the distribution coefficient of magnetic force in axial direction, the magnetic forces generated by four pairs of axial AMAs are used to the suspension control of A-gimbal in axial direction, and the residual magnetic forces generated by four axial AMAs are used to control the attitude angles of A-gimbal. The four radial AMAs are separated as two groups and working in pairs to generate the magnetic forces for the radial suspension of A-gimbal.

In the power amplification model, the plus width modulation (PWM) type current amplifiers are used to generate the control currents of windings. The relationship between the control signal and the control current could be described as follows

$$\boldsymbol{I}(s) = P(s)\boldsymbol{U_I}(s) \tag{24}$$

where $\boldsymbol{P}(s)$ is the transfer function of power amplification model with a two-order linear system.

Furthermore, the control currents could drive the windings of the axial-radial integrated AMA system to generated the magnetic forces and the gimbal torques according to (10), (11) and (12).

Tracking control of closed-loop system

As shown in Fig. 7(b), a tracking control model is used to adjust the information attitude of A-gimbal. The attitude information [α_g β_g θ_g] in the geographic coordinate frame could be measured by the POS, and the attitude information of the P-gimbal and the R-gimbal could be measured by the accelerators mounted on gimbals. The actual attitude information of A-gimbal could be obtained by the coordinate transformation in (16), and a PD control model is used in the tracking control model.

Simulation of MS-ISP

The suspension simulation of AMA system

The simulations are conduced to test the performances of AMA system and the A-gimbal before the experiment. Firstly, the suspension abilities of AMA system along three axes are tested, and the levitation traces of A-gimbal suspended by the magnetic forces of AMA system are shown in Fig. 8. The levitation traces of A-gimbal in radial direction are plotted in the red line in Fig. 8(a) and (b), and the A-gimbal could be levitated to the radial equilibrium position when the initial displacement sets at 0.05 mm in radial direction. In Fig. 8(c), although there is obvious overshoot term because of the self-weight in axial direction, the A-gimbal could be levitated to the axial equilibrium position.
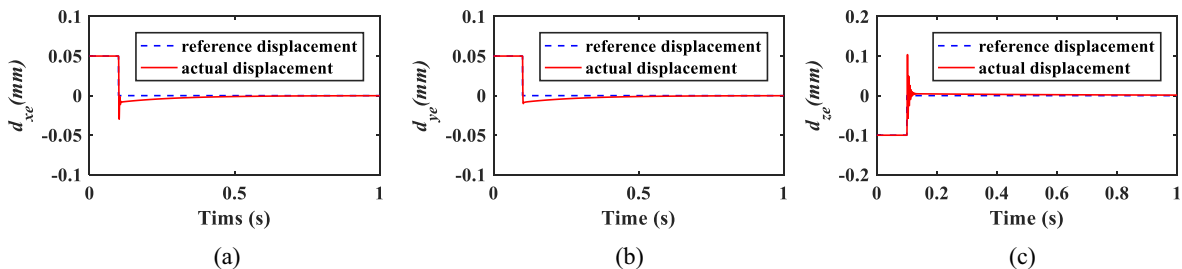

Fig. 8. The suspension simulation of A-gimbal suspended by AMA system, (a) the levitation trace of A-gimbal in X_e axis, (b) the levitation trace of A-gimbal in Y_e axis, (c) the levitation trace of A-gimbal in Z_e axis.
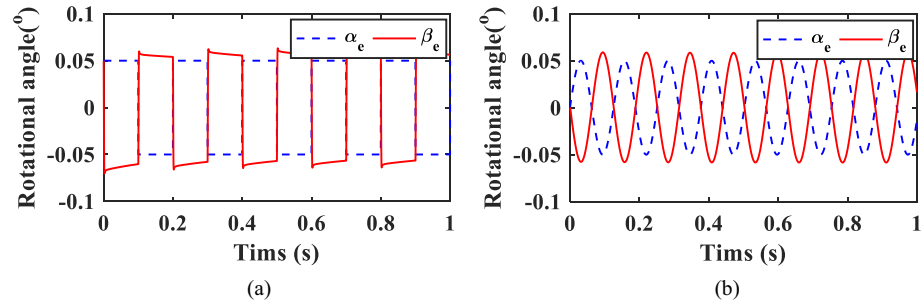
Fig. 9. The tracking performance of A-gimbal suspended by AMA system, (a) the tracking curves for square signal, (b) the tracking curves for sinusoidal signal.
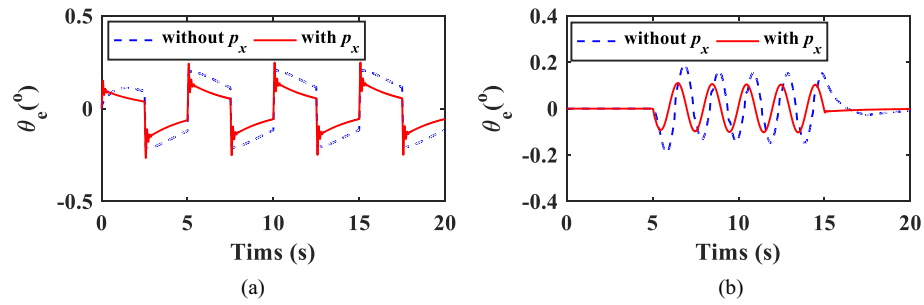

Fig. 10. (a) The tracking curve of A-gimbal's yaw angle θ_e for square signal, (b) the tracking curve of A-gimbal's yaw angle θ_e for sinusoidal signal.
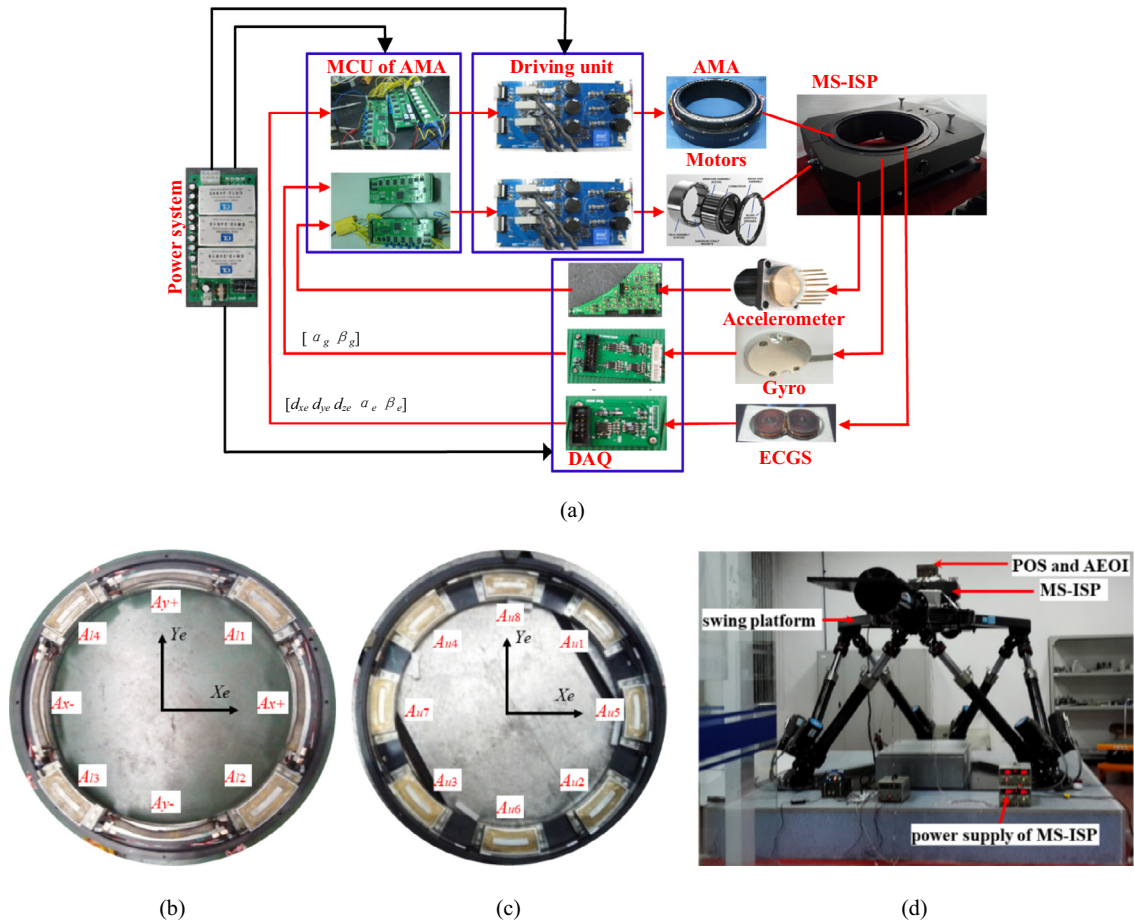

Fig. 11. (a) The experimental setup of whole MS-ISP system, (b) the AMA system at lower end-face, (c) the AMA system at lower end-face, (d) the experimental setup of MS-ISP on the swing platform.

Table 1
System parameters of the MS-ISP.

Symbol	Quantity	Value
l_s	diameter of the A-gimbal	450 mm
k_{ix}	radial current stiffness	300 N/A
k_{dx}	radial displacement stiffness	−650 N/mm
k_{iz}	axial current stiffness	1300 N/A
k_{dz}	axial displacement stiffness	−3600 N/mm
k_{ipx}	current stiffness of gimbal torque	88.2Nm/A
k_{dpx}	displacement stiffness of gimbal torque	−78Nm/deg
k_s	sensitivity of ECGS	3 V/mm
k_a	amplification coefficient of power module	0.2A/V
K_p	proportional coefficient of stabilization loop	3.5
K_i	integral coefficient of stabilization loop	0.01
K_d	derivative coefficient of stabilization loop	2.6
K_{pt}	proportional coefficient of tracking loop	3.6
K_{dt}	derivative coefficient of tracking loop	0.2
	control frequency of AMA system	10 kHz
	control frequency of servo-drive motor	2 kHz

Moreover, the tracking performance of AMA system is also tested in the simulation, and the tracking curves for the square signal and sinusoidal signal are plotted in Fig. 9. When the reference signal is chosen a square signal with 0.05°and 0.2 s, the tracking curves of A-gimbal with AMA system is shown in Fig. 9(a), and the error is about 0.001°. The tracking curve is illustrated in Fig. 9(b) when the reference signal is sinusoidal signal with 0.05°and 0.2 s, and the actual tilting angles of A-gimbal could accurately track the reference input with 0.001° error.

The tracking simulation of A-gimbal

The tracking simulation of A-gimbal driven by the servo-drive motor around Z_e axis is also conducted. For the tracking curve of square signal (amplitude is 0.1° and period is 5 s) in Fig. 10(a), the tracking error of A-gimbal with using the gimbal torque p_x as shown in the blue line is 0.06°, but that with using the gimbal torque is reduced to 0.03°. For the tracking curve of sinusoidal signal
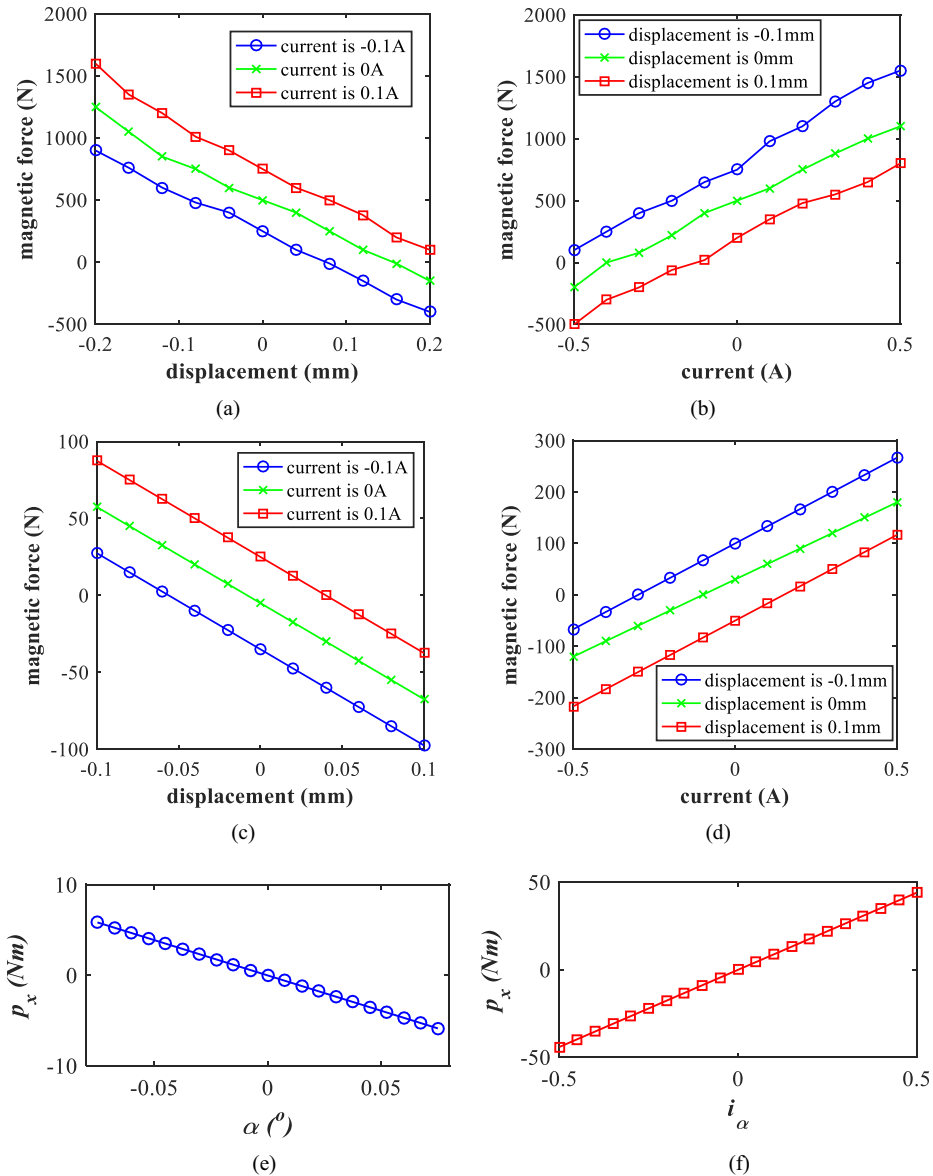

Fig. 12. (a) The magnetic force versus control displacement in axial direction, (b) the magnetic force versus control current in axial direction, (c) the magnetic force versus control displacement in radial direction, (d) the magnetic force versus control current in radial direction, (e) the gimbal torque versus the rotational angle, (f) the gimbal torque versus the control current.

(amplitude is 0.1° and period is 2 s) in Fig. 10(b), the tracking error without applying the gimbal torques is 0.03°, but the tracking error is declined to 0.005° by using the gimbal torques. Therefore, the gimbal torques of AMA system could improve the tracking precision of A-gimbal by suppressing the disturbance acting on it.

Performance analysis of MS-ISP

Experimental setup

The prototype of MS-ISP with an axial-radial integrated AMA system is described in Fig. 11(a). In detail, the accelerometers and the rate gyros could measure the attitude information of three gimbals in the MS-ISP. The power supply system could output power voltage for MS-ISP system including ± 5 V for the MCU, ±12 V for the data acquisition (DAQ) module and ± 28 V for the axial-radial integrated AMA system. The DAQ system could collect the signals of MS-ISP and fed back to the MCU system. For the MCU, a digital control system based on the digital signal processor (DSP) is designed to realize the program of designed control models. The MCU system consists of the ECGS, the measuring circuit of coil current, the signal filter and conditioner, the DSP core, the analog to digital (A/D) convertor, the current amplifier and the communication module. The A/D sampling rate and control cycle are 5 kHz, and the PWM modulation frequency of driving unit is 20 kHz. The more parameters of MS-ISP are listed in Table 1.

Magnetic forces and gimbal torques of axial-radial integrated AMA system

The magnetic forces generated by the axial-radial integrated AMA system could be calculated and measured in the experiment. In axial direction, the relationships amongst the magnetic force, the control displacement and the control current are shown in Fig. 12. Given the condition that the control current is 0A in Fig. 12(a), the linear displacement stiffness is about −3600 N/mm. When the control displacement is 0 mm as shown in Fig. 12(b), the linear current stiffness is about 1300 N/A. Moreover, the relationships amongst the radial magnetic force, the control displacement and the control current are illustrated in Fig. 12(c) and (d). The linear displacement stiffness in Fig. 12(c) is −650 N/mm, and the linear current stiffness in Fig. 12(d) is 300 N/A.

Based on the axial current stiffness and the axial displacement stiffness of the axial-radial integrated AMA system, the relationships amongst the rotational angle, the control current and the gimbal torque acting on the A-gimbal are plotted in Fig. 12(e)
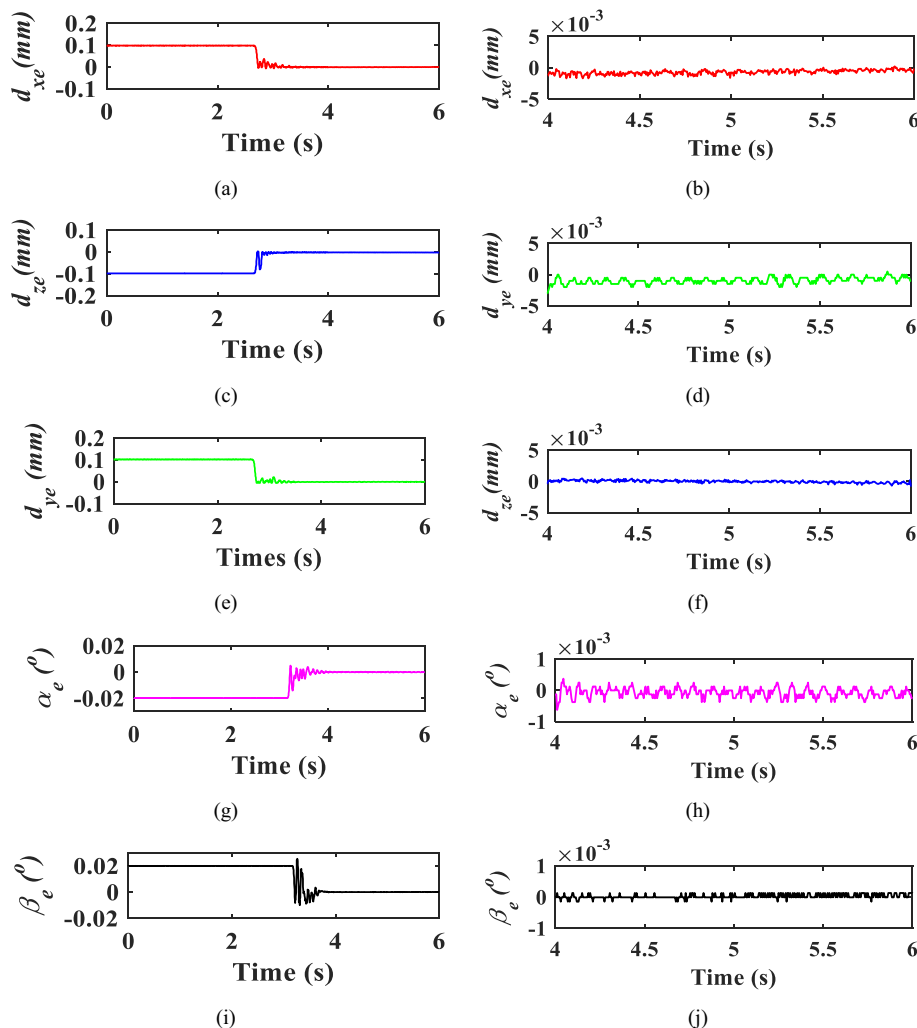

Fig. 13. (a) The levitation trace of A-gimbal in X_e axis, (b) steady-state suspension trace of A-gimbal in X_e axis, (c) levitation trace of A-gimbal in Y_e axis, (d) steady-state suspension trace of A-gimbal in Y_e axis, (e) levitation trace of A-gimbal in Z_e axis, (f) steady-state suspension trace of A-gimbal in Z_e axis, (h) rotational trace of A-gimbal around X_e axis, (h) steady-state rotational stabilization of A-gimbal around X_e axis, (i) rotational trace of A-gimbal around Y_e axis, (j) steady-state rotational stabilization of A-gimbal around Y_e axis.

and (f). The gimbal torque generated by the axial-radial integrated AMA system is linear to the rotational angle and the control current, respectively. The current stiffness of gimbal torque is 88.2Nm/A, and the angle stiffness of gimbal torque is −78Nm/deg. Therefore, the gimbal torque acting on the A-gimbal has good linearity by regulating the control current.

Static suspension of A-gimbal

As shown in Fig. 13, the A-gimbal is stably levitated at the equilibrium positions in axial and radial directions. The initial displacement terms of A-gimbal are chosen as $[d_{xe}\ d_{ye}\ d_{ze}\ \alpha_e\ \beta_e]$ = [0.1 mm 0.1 mm −0.1 mm −0.02° 0.02°], and the A-gimbal is forced to suspended at the equilibrium positions when the displacement terms $[d_{xe}\ d_{ye}\ d_{ze}\ \alpha_e\ \beta_e]$ = [0 mm 0 mm 0 mm 0° 0°] with the function of the axial-radial integrated AMA system. For the translational suspension of A-gimbal shown in Fig. 13(a), (c) and (e), the maximum overshoot with 0.08 mm occurs on suspension trace in axial direction, and the settling time is 0.8 s. For the rotational traces of A-gimbal shown in Fig. 13(g) and (i), the maximum overshoot 0.024° occurs on the rotational trace around Y_e axis, and the settling time is 0.8 s. Finally,

the A-gimbal could be stably suspended at the equilibrium positions by the axial-radial integrated AMA system.

Moreover, the stable suspension traces of A-gimbal on five controllable DOFs are plotted in Fig. 13. For the translational displacements of A-gimbal in radial and axial directions, the steady-state precision is evaluated by the root mean square (RMS) value when the A-gimbal is at the balanced status. As illustrated in Fig. 13(b), (d) and (f), the steady-state precisions of A-gimbal along three axes are 0.77 μm, 1.1 μm and 0.29 μm; respectively. In addition, the steady-state precisions of rotational motions are $0.17°×10^{-3}$ and $0.08°×10^{-3}$; separately. The steady-state precision in translational motion is less than 2 μm, and that of rotational motion is smaller than $0.2°×10^{-3}$, so the A-gimbal with an axial-radial integrated AMA system has a better stabilization precision than the mechanical supporting gimbal (the steady-state precision is 0.02°).

The bandwidth of axial-radial integrated AMA system

To evaluate the dynamic response of MS-ISP, the bandwidth of the axial-radial integrated AMA system is analyzed in this section. The reference sinusoidal signal in pitch rotation varies from 1 Hz to
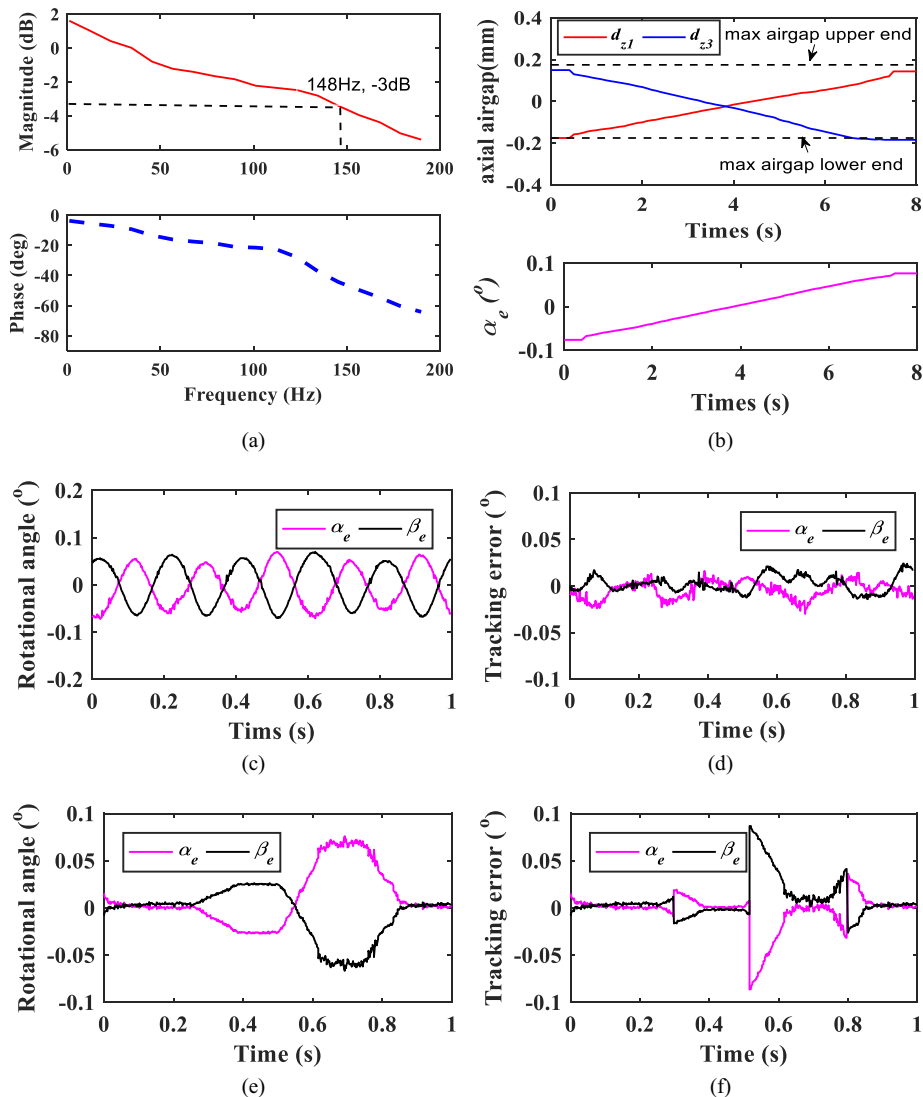

Fig. 14. (a) The bandwidth of axial-radial integrated AMA system, (b) rotational curves and airgaps of A-gimbal around X_e axis, (c) tracking curves for sinusoidal signal, (d) tracking errors for sinusoidal signal, (e) tracking curves for step signal, (f) tracking errors for step signal.
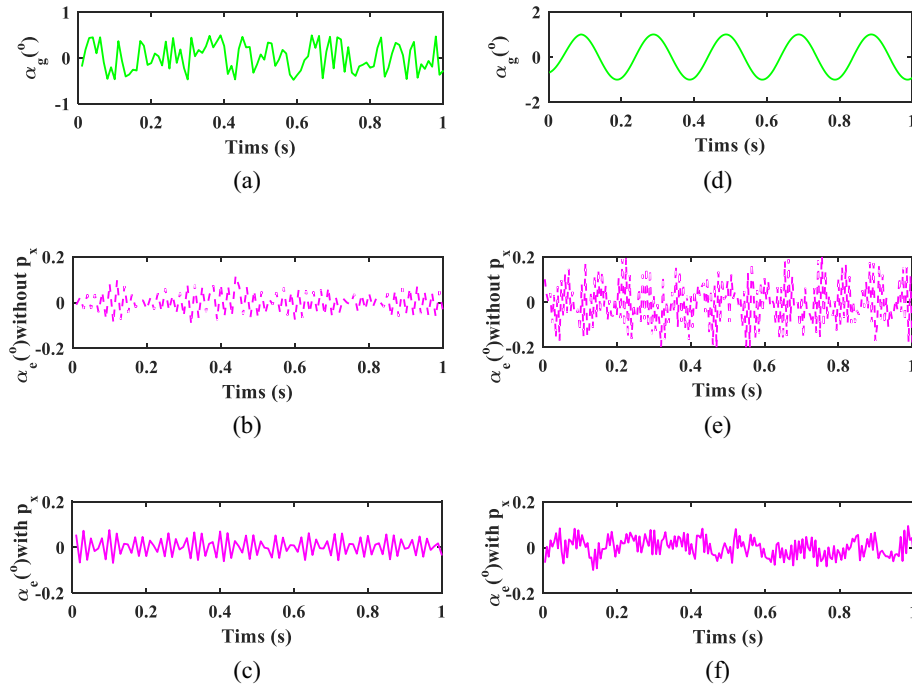
Fig. 15. (a) The random-type vibration curve, (b) the attitude curve of A-gimbal α_e without using gimbal torque p_x, (c) the attitude curve of A-gimbal α_e with using gimbal torque p_x, (d) sine-type vibration curve, (e) the attitude curve of A-gimbal α_e without using gimbal torque p_x, (f) the attitude curve of A-gimbal α_e with using gimbal torque p_x.

180 Hz, and the amplitude-frequency diagram and the phase-frequency diagram are plotted in Fig. 14(a). When the frequency approaches to 150 Hz, the response magnitude is −3dB, so the bandwidth of axial-radial integrated AMA system beyond 100 Hz. Therefore, the major disturbances (from 0 Hz to 100 Hz) acting on the rotations and translations of the A-gimbal could be actively controlled by the axial-radial integrated AMA system.

The tracking performance of suspended A-gimbal

The rotational characteristics of axial-radial integrated AMA system are also tested within the tolerant airgap (0.2 mm) in axial direction. The axial displacements during the rotation process are plotted in Fig. 14(b), and the maximum displacement deflection of A-gimbal in axial direction is 0.185 mm. The corresponding rotational angle α_e during the rotation process is illustrated in Fig. 14 (b), and the maximum rotational angel approaches to 0.075° when the axial displacement reaches to the tolerant airgap. Similarly, the characteristics about rotational angle β_e could be investigated. So, the active controllability of axial-radial integrated AMA system could be realized within the axial tolerant airgap.

The attitude tracking performance of A-gimbal with an axial-radial integrated AMA system is also tested in this part. As shown in Fig. 14(c), the rotations of A-gimbal relative to P-gimbal are forced to track a sinusoidal signal (frequency is 5 Hz and amplitude is 0.06°), and the tracking curves indicate that the A-gimbal could stably track the reference curve. Moreover, the tracking errors of two rotations are plotted in Fig. 14(d), for the rotational angle α_e around X_e axis, the steady-state error is about 0.0099°, and the steady-state error of rotational angle β_e around Y_e axis is 0.0089°. Therefore, the A-gimbal with an axial-radial integrated AMA system could accurately track the reference input, so it could be successfully applied to track the pitch and roll rotation of the A-gimbal.

In addition, the tracking curves of A-gimbal for a continual step signal (variable amplitude) are plotted in Fig. 14(e). The slight time-lag about 0.1 s exists on the tracking curves of two rotations.

In the meanwhile, the tracking errors are shown in Fig. 14(f), and the maximum tracking error appears when the continual step signal jumps to another amplitude. The tracking error also increases with the magnitude variation of step signal, and the maximum tracking error is about 0.5° in Fig. 14(f).

Attitude stabilization performance of A-gimbal on swing platform

In the dynamic experiment of MS-ISP on the ground, the MS-ISP is mounted on a swing platform as shown in Fig. 11(d), and a random-type disturbance with amplitude 0.5° in Fig. 15(a) is outputted to the base plate of MS-ISP by controlling the swing platform. When the gimbal torque p_x is not applied to compensate the pitch rotation and the roll rotation, the attitude curve of A-gimbal is shown in Fig. 15(b), and the RMS of the A-gimbal's attitude curve is 0.0508°. As illustrated in Fig. 15(c), the RMS of A-gimbal's attitude angle is reduced to 0.0396° by using the gimbal torque p_x, and then the relative improvement is about 22%.
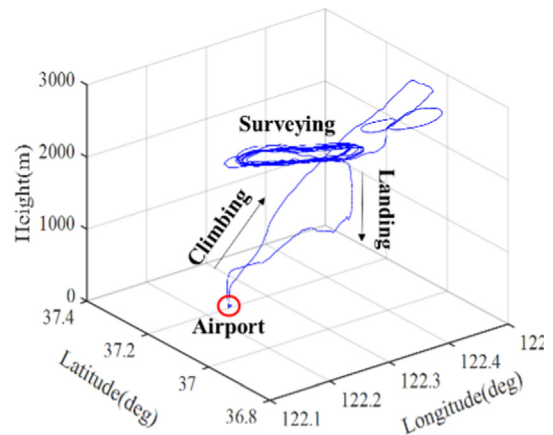

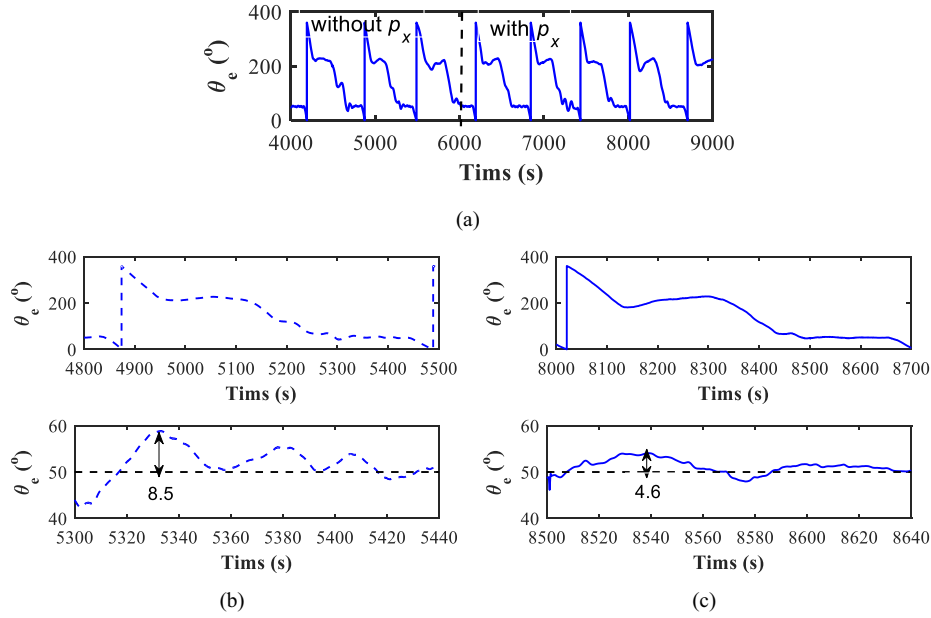**Fig. 16.** The flight path during the flight experiment.

Fig. 17. (a) The attitude curve of A-gimbal driven by servo-drive motor, (b) the attitude curve of A-gimbal θ_e without using gimbal torque p_x, (c) the attitude curve of A-gimbal θ_e with using gimbal torque p_x.
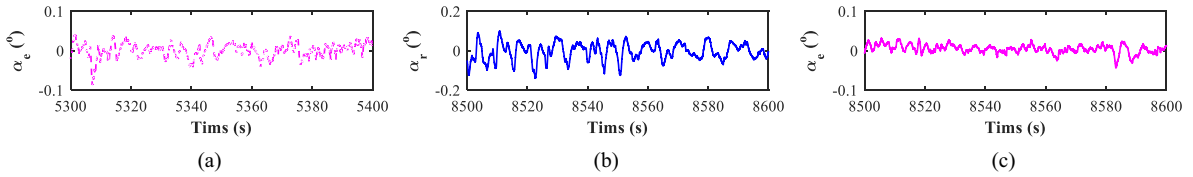

Fig. 18. (a) The attitude curve of A-gimbal α_e without using gimbal torque p_x, (b) the attitude curve of R-gimbal α_r without using gimbal torque p_x, (c) the attitude curve of A-gimbal α_e with using gimbal torque p_x.

In addition, a sine-type disturbance with amplitude 1° and period 5 Hz in Fig. 15(e) is generated to the base plate of MS-ISP by tuning the swing platform. As shown in Fig. 15(d), the RMS of A-gimbal's attitude angle is 0.1067° when the gimbal torque p_x is not applied to compensate the rotation motion. In Fig. 15(f), the RMS of A-gimbal's attitude is reduced to 0.0414° by using the gimbal torque p_x, and then the relative improvement is about 60%.

Attitude stabilization performance of A-gimbal in flight

In the flight experiment of MS-ISP, the flight path is plotted in Fig. 16. The whole flight task includes three processes—climbing process, surveying process and landing process. The MS-ISP is switched on during the surveying process at 2000 m altitude, and the whole surveying task is about 2 h.

During the surveying process, the yaw angle θ_e of A-gimbal around Z_e axis controlled by the drive-servo motor is plotted in Fig. 17(a). The yaw angle θ_e is regulated from 360° to 0° with two stable stages respectively at 50° and 200° during the whole surveying process. The gimbal torque is introduced to suppress the pitch and roll rotation acting on the yaw rotation of A-gimbal when the task time is at 1 h. Furthermore, in Fig. 17(b), for the attitude curve θ_e of A-gimbal without using gimbal torque, the maximum error deflecting from the stable magnitude is 8.5°. For the attitude curve θ_e of A-gimbal using the gimbal torque as shown in Fig. 17(c), the maximum error deflecting from the equilibrium magnitude is 4.6°. Therefore, the maximum angle error of yaw rotation is reduced 44.8% by applying the gimbal torque of the axial-radial integrated AMA system.

Moreover, the attitude angles α_e and α_r are recorded and plotted in Fig. 18(a), (b) and (c), and α_e is the rotational angle of A-gimbal around X_e axis, α_r is the rotational angle of R-gimbal around Z_e axis. When the gimbal torque p_x generated by the axial-radial integrated AMA system is not used to compensate the pitch and roll rotation of A-gimbal, the attitude curve of yaw angle α_e is plotted in Fig. 18 (a), and the RMS of rotational angle α_e is 0.0181°. The attitude curve α_r of R-gimbal with the supporting of mechanical bearings is illustrated in Fig. 18(b), and its RMS is 0.0443°. Finally, the attitude angle α_e of A-gimbal is presented in Fig. 18(c) when the gimbal torque p_x is used, and the RMS is 0.0118°. Consequently, the attitude stabilization precision of levitated A-gimbal with the gimbal torque generated by the axial-radial integrated AMA system is improved by 93%.

Conclusions

A prototype of MS-ISP has been introduced and designed in this article. The A-gimbal of MS-ISP is stably suspended at the equilibrium positions by an axial-radial integrated AMA system. In addition, the tracking performance of A-gimbal indicates that the axial-radial integrated AMA system could generate the gimbal torques to accurately track the rotations around the P-gimbal and the R-gimbal, and the steady-state error is less than 0.01°. In the meanwhile, the bandwidth of the axial-radial integrated AMA system could cover the frequency range of disturbances acting on the A-gimbal. In the flight experiment, the high attitude stabilization precision of A-gimbal could timely track the LOS of AEOI. Therefore, the MS-ISP is potential to be applied in the remote sensing system,

and then the attitude stabilization of payloads and ISP could be improved.

Declaration of Competing Interest

The authors declared that there is no conflict of interest.

References

[1] Hilkert J. Inertially stabilized platform technology concepts and principles. IEEE Control Syst 2008;28:26–46.

[2] Masten MK. Inertially stabilized platforms for optical imaging systems. IEEE Control Syst 2008;28:47–64.

[3] Wang HG, Williams TC. Strategic inertial navigation systems - high-accuracy inertially stabilized platforms for hostile environments. IEEE Control Syst 2008;28:65–85.

[4] Zhou X, Shi Y, Li L, Yu R, Zhao L. A High Precision Compound Control Scheme Based on Non-singular Terminal Sliding Mode and Extended State Observer for an Aerial Inertially Stabilized Platform. Int J Control Autom Syst 2020:1–12.

[5] Wang F, Wang R, Liu E, Zhang W. Stabilization Control Mothed for Two-Axis Inertially Stabilized Platform Based on Active Disturbance Rejection Control With Noise Reduction Disturbance Observer. Access 2019;7:99521–9.

[6] Mao J, Yang J, Liu X, Li S, Li Q. Modeling and Robust Continuous TSM Control for an Inertially Stabilized Platform With Couplings. IEEE Trans Control Syst Technol 2019.

[7] Mao J, Li S, Li Q, Yang J. Design and implementation of continuous finite-time sliding mode control for 2-DOF inertially stabilized platform subject to multiple disturbances. ISA Trans 2019;84:214–24.

[8] Chen X, Fang F, Luo X. A friction identification approach based on dual-relay feedback configuration with application to an inertially stabilized platform. Mechatronics 2014;24:1120–31.

[9] Cong S, Deng K, Shang W, Kong D, Shen H. Isolation control for inertially stabilized platform based on nonlinear friction compensation. Nonlinear Dyn 2016;84:1123–33.

[10] Wen T, Xiang B, Wong W. Coupling Analysis and Cross-Feedback Control of Three-Axis Inertially Stabilized Platform with an Active Magnetic Bearing System. Shock Vib 2020;2020:8290369.

[11] Zhou X, Gong G, Li J, Zhang H, Yu R. Decoupling control for a three-axis inertially stabilized platform used for aerial remote sensing. Trans Inst Meas Control 2015;37:1135–45.

[12] Fang J, Yin R, Lei X. An adaptive decoupling control for three-axis gyro stabilized platform based on neural networks. Mechatronics 2015;27:38–46.

[13] Tong W, Xiang B, Wong W. Gimbal torque and coupling torque of six degrees of freedom magnetically suspended yaw gimbal. Int J Mech Sci 2020;168:105312.

[14] Moorty JK, Marathe R. H∞ control law for line-of-sight stabilization for mobile land vehicles. Opt Eng 2002;41:2935–44.

[15] Darestani MR, Nikkhah AA, Sedigh AK. H∞/Predictive output control of a three-axis gyrostabilized platform. Proc Institution Mechanical Engineers, Part G: J Aerospace Engineering 2014;228:679–89.

[16] Khodadadi H, Motlagh M, Gorji M. Robust control and modeling a 2-DOF Inertial Stabilized Platform, in. International Conference on Electrical 2011.

[17] Lin F-J, Shen P-H. Robust fuzzy neural network sliding-mode control for two-axis motion control system. IEEE Trans Ind Electron 2006;53:1209–25.

[18] Safa A, Abdolmalaki RY. Robust output feedback tracking control for inertially stabilized platforms with matched and unmatched uncertainties. IEEE Trans Control Syst Technol 2017;27:118–31.

[19] Guo Q, Liu G, Xiang B, Wen T, Liu H. Robust control of magnetically suspended gimbals in inertial stabilized platform with wide load range. Mechatronics 2016;39:127–35.

[20] O. Sushchenko, Robust Control of Inertially Stabilized Platforms for Ground Vehicles on the Basis of Synthesis, Proceedings of the National aviation university, (2016) 24–34-24–34.

[21] Safa A, Abdolmalaki RY. Robust Output Feedback Tracking Control for Inertially Stabilized Platforms With Matched and Unmatched Uncertainties. IEEE Trans Control Syst Technol 2017.

[22] Lei X, Zou Y, Dong F. A composite control method based on the adaptive RBFNN feedback control and the ESO for two-axis inertially stabilized platforms. ISA Trans 2015;59:424–33.

[23] Zhou X, Jia Y, Zhao Q, Cai T. Dual-rate-loop control based on disturbance observer of angular acceleration for a three-axis aerial inertially stabilized platform. ISA Trans 2016;63:288–98.

[24] Yu S, Zhao Y. Simulation study on a friction compensation method for the inertial platform based on the disturbance observer. Proc Institution Mechanical Engineers, Part G: J Aerospace Engineering 2008;222:341–6.

[25] Guo Q, Liu G, Xiang B, Liu H, Wen T. The disturbance rejection of magnetically suspended inertially stabilized platform. Trans Inst Meas Control 2018;40:565–77.

[26] B. Xiang, W. on Wong, Vibration characteristics analysis of magnetically suspended rotor in flywheel energy storage system, Journal of Sound and Vibration, 444 (2019) 235-247.

[27] Ahrens M, Kucera L, Larsonneur R. Performance of a magnetically suspended flywheel energy storage device. IEEE Trans Control Syst Technol 1996;4:494–502.

[28] Xiang B, Tang J. Suspension and titling of vernier-gimballing magnetically suspended flywheel with conical magnetic bearing and Lorentz magnetic bearing. Mechatronics 2015;28:46–54.

[29] T. Masuzawa, Magnetically suspended motor system applied to artificial hearts and blood pumps, Proceedings of the Institution of Mechanical Engineers, Part I: Journal of Systems and Control Engineering, 231 (2017) 330-338.

[30] Paul G, Rezaienia MA, Rahideh A, Munjiza A, Korakianitis T. The effects of ambulatory accelerations on the stability of a magnetically suspended impeller for an implantable blood pump. Artif Organs 2016;40:867–76.

[31] Melin AM, Kisner RA. Design and Analysis of Embedded I&C for a Fully Submerged Magnetically Suspended Impeller Pump. Nucl Technol 2018;202:180–90.

[32] Xiang B, Wong W. Electromagnetic vibration absorber for torsional vibration in high speed rotational machine. Mech Syst Sig Process 2020;140.